Effect of water content and structural anisotropy on tensile mechanical properties of montmorillonite using molecular dynamics

Pengchang Wei, Yuan-Yuan Zheng, Yong Xiong, Shengbiao Zhou, Kamal Al-Zaoari, Ali Zaoui

Effect of Water Content and Structural Anisotropy on Tensile Mechanical Properties of Montmorillonite using Molecular Dynamics

Pengchang WEI [a,b], Yuan-Yuan ZHENG [*,a,b], Yong XIONG [a], Shengbiao ZHOU [a], Kamal Al-Zaoari [a], Ali ZAOUI [b]

[a] School of Civil Engineering, Sun Yat-Sen University, Guangzhou, 510275, China & Southern Marine Science and Engineering Guangdong Laboratory (Zhuhai), Zhuhai, 519082, China

[b] Univ. Lille, IMT Lille Douai, JUNIA, Univ. Artois, ULR 4515 - LGCgE, Laboratoire de Génie Civil et géo-Environnement, F-59000 Lille, France

[*] Corresponding author: Dr. Yuan-Yuan ZHENG, Tel.: +86 180 2245 0508.

E-mail: zhengyy57@mail.sysu.edu.cn; zyy378@hotmail.fr

Address: School of Civil Engineering, Zhuhai Campus of Sun Yat-Sen University, Tang Jia Wan, Zhuhai City, 519082, P. R. China

Abstract:

The mechanical behavior of montmorillonite is sensitive to water content and structural anisotropy. In this study, the evolution of atomic structure and mechanical behavior of different hydrated montmorillonite under tension has been investigated using Molecular Dynamics simulations. External deformation has been applied to montmorillonite with a strain rate of 5×10^{-7} fs^{-1} for uniaxial tensile test, stretched along directions parallel (*x*- and *y*-direction) and perpendicular (*z*-direction) to the clay sheets. The bond-breakage criterion based on the radial distribution function of atom pairs and the evolution of broken bonds with tensile strain, were applied to explore the deformation and failure mechanism of the montmorillonite-water system. Simulation results indicated that the water content increased, causing a decrease in the ultimate tensile strength and Young's modulus, as well as more and more plasticity for montmorillonite, especially in *z*-direction. Moreover, the sequence of tensile mechanical strength was $y > x > z$. Stretching along the *x*- and *y*-direction, fractures occurred in the silicon-oxygen tetrahedral and aluminum-oxygen octahedral sheets, where the aluminum-oxygen bond was easier to be broken, and the normalized number of total broken bonds in the *y*-direction was superior to the *x*-direction. Stretching along the *z*-direction, only the hydrogen bonds in the interlaminar space were broken. In terms of three directions, the anisotropy behavior was found in ultimate tensile strength, Young's modulus, residual tensile strength, and the evolution of broken bonds.

Keywords: Montmorillonite; Molecular Dynamics; Water content; Tensile Mechanical properties; Structural Anisotropy; Microstructure

1. Introduction

Clay minerals are widely distributed on the earth, and are the principal components of swelling clay and claystone. The mechanical properties of clay minerals are always decisive to the macroscopic properties of clay and claystone, which have been widely studied in geotechnical engineering (Zheng et al., 2011; Liu et al., 2019; Yotsuji et al., 2021). As is well known, the mechanical properties of clay minerals are very sensitive to water content and structural anisotropy (Zhang et al., 2012; Liu et al., 2015; Zheng and Zaoui, 2018). So far, plenty of experimental measurements (Mcneil and Grimsditch, 1993; Vanorio et al., 2003; Bobko and Ulm, 2008; Nazmul et al., 2008; Hedan et al., 2015; Húlan et al., 2015) and theoretical derivation methods (Hueckel, 2002; Chen and Evans, 2006; Ortega et al., 2007) have been used to study the structural and mechanical properties of claystone and clay minerals, such as the Brillouin scattering method (Mcneil and Grimsditch, 1993), acoustic measurement (Vanorio et al., 2003), nano-indentation test (Bobko and Ulm, 2008; Wu et al., 2020), in-situ test (Húlan et al., 2015), high energy synchrotron X-ray, and the crystallographic Rietveld method (Wenk et al., 2007). These previous works showed that the mechanical strength of clay minerals declined with increasing water content, and showed obvious anisotropy in mechanical strength and failure form. On the other hand, the macroscopic deformation of claystone is controlled by the local motion of clay particles at different scales (Zhu et al., 2021). The macroscopic mechanical properties of claystone are strongly sensitive to water saturation degree (Zhang et al., 2012). The microscopic mechanical behavior of clay particles also depends on the hydration in interlayer spacing. Therefore, in terms of clays, especially swelling clay, a fundamental molecular-level understanding of the clay-water interaction plays a significant role in the evolution of its microstructure, hydromechanical behavior, and development of multiscale approaches (Katti et al., 2007).

The first-principles and molecular dynamics (MD) simulation methods have been used to study the nanoscale mechanical behaviors of clay minerals. The first-principles simulation method has been

used to study the microstructure (Stixrude and Peacor, 2002), bulk modulus, and elastic constant (Sato, 2005; Militzer et al., 2010) of clay minerals. Although the first-principles method is powerful and reliable in the simulation results, the number of atoms in the studied system is limited due to the important computational burden. MD simulation method is a well-established tool to model up to millions of atoms and observe the system's deformation and failure details in nanoscale (Yang et al., 2019; Wei et al., 2022). The MD simulation method has been widely performed to investigate the elastic and structural properties of montmorillonite (Manevitch and Rutledge, 2004; Suter et al., 2007; Ebrahimi et al., 2012), illite (Hantal et al., 2014), kaolinite (Benazzouz and Zaoui, 2012), muscovite (Teich-McGoldrick et al., 2012), etc. Schmidt et al. (Schmidt et al., 2005) explored the evolution of the mechanical response of Na-montmorillonite interlayer with increasing hydration. Mazo et al. (Mazo et al., 2008) found that the elastic modulus of montmorillonite containing monolayer water molecules is more significant than that with bilayer water molecules. Recently, the mechanical behavior of dehydrated kaolinite under tensile and compression has been studied in previous works (Zhang et al., 2021), and Yang et al. (Han et al., 2019; Yang et al., 2019) also considered the effect of temperature and hydrated state on that of kaolinite. Furthermore, the effect of loading path and orientation on mechanical behaviors for dehydrated Na-montmorillonite has been explored, while ignoring hydration (Zhu et al., 2021). Katti et al. (Katti et al., 2007) reported the mechanical response of the interlayer of dehydrated and hydrated montmorillonite using steered MD simulation, and Zhang et al. (Zhang et al., 2012) explored the effect of water content and structural anisotropy on the mechanical property of claystone via micro-indentation and mini-compression tests. The above research has well advanced the knowledge of the structural and mechanical properties of clay minerals. However, some interesting questions arise: How many bonds would be broken in the montmorillonite system in the deformation and failure process? And which bond breaks first? How does the structural anisotropy of montmorillonite and its hydrated state affect the evolution of bond-breakage and tensile mechanical behavior?

To the end, MD simulations have been used to investigate the structure and mechanical properties of hydrated montmorillonite under tension. In the CLAYFF force field, a bond-breakage criterion based on radial distribution function (RDF) of atom pairs would be performed to describe the evolution of bond-breakage during the failure process of montmorillonite, considering Al…O, Si…O, and O…H bonds. Furthermore, the effect of water content on stress-strain curve, ultimate tensile strength, Young's modulus, and residual tensile strength of montmorillonite are evaluated.

2. Simulation details

2.1. System setup and force field

The Wyoming-type montmorillonite is a 2:1 type clay mineral, with one aluminum-oxygen octahedral sheet sandwiched between two silicon-oxygen tetrahedral sheets. The simulation model was derived from Viani et al. (Viani et al., 2002), with the chemical formula of unit cell as $Na_{0.75}(Si_{7.75}Al_{0.25})(Al_{3.5}Mg_{0.5})O_{20}(OH)_4 \cdot nH_2O$. The lattice substitution of montmorillonite was performed based on the following principles: (1) Adjacent atoms cannot be replaced at the same time; (2) One out of every eight Al^{3+} is replaced by Mg^{2+} in the octahedral sheet, and one out of every 32 Si^{4+} in the tetrahedral sheet is replaced by Al^{3+}, where the replacement positions are randomly distributed on the upper and lower layers of the clay sheet. The basal spacing of montmorillonite was adjusted from an initial 15.0 Å to 9.6, 11.0, 12.5, and 14.0 Å, corresponding to the system with water contents of 0%, 10%, 20%, and 30% weight percent, respectively. Water molecules were distributed randomly in the interlayer space of montmorillonite. Thereafter, the supercells of montmorillonite are composed of 128 unit cells ($8a \times 4b \times 4c$), as shown in Figure 1. Moreover, the water molecules in this system were represented by the rigid SPC/E water model (Berendsen et al., 1987), which was adopted to describe interactions among hydrated montmorillonite.

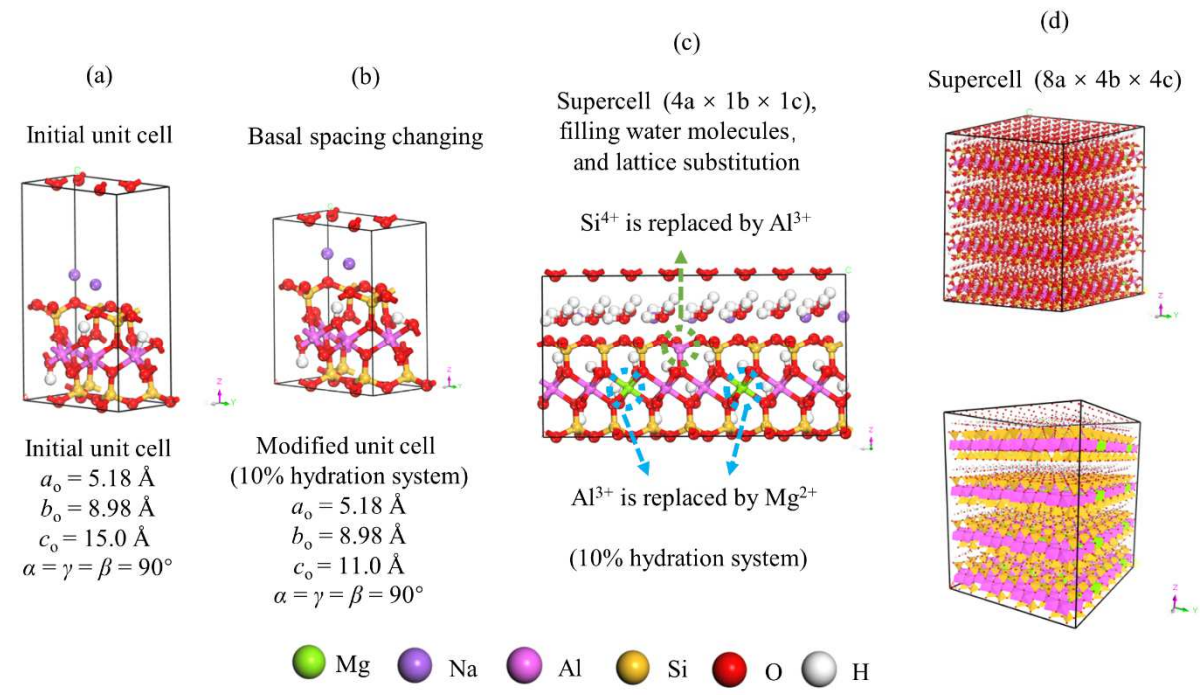

Figure 1. Modeling process of Na-montmorillonite system.

CLAYFF (Cygan et al., 2004) force field has been widely used for clay minerals in MD simulation (Seppälä et al., 2016; Zheng and Zaoui, 2018; Wei et al., 2021; Al-Zaoari et al., 2022), which was applied in this work. The non-bonded and bonded interaction parameters of the CLAYFF force field were derived from the literature (Cygan et al., 2004), where Lennard-Jones parameters of montmorillonite-water system are shown in Table 1. The total potential energy (E_{total}) of the system could be calculated by equation (1).

$$E_{\text{total}} = E_{\text{bond stretch}} + E_{\text{Coulomb}} + E_{\text{VDW}}$$
$$= k_1(r_{ij} - r_0)^2 + \frac{e^2 q_i q_j}{4\pi\varepsilon_0 r_{ij}} + 4\varepsilon_{ij}\left[\left(\frac{\sigma_{ij}}{r_{ij}}\right)^{12} - \left(\frac{\sigma_{ij}}{r_{ij}}\right)^{6}\right] \quad (1)$$

where k_1 is the force constants, and r_0 represents the equilibrium bond length; r_{ij} is the distance between atoms i and j; q_i and q_j are the charges of atoms i and j, respectively; ε_0 is the dielectric constant; σ and ε are the size and energy parameters, respectively. Moreover, σ_{ij} and ε_{ij} can be obtained by Mixing Lorentz-Berthelot's law (Frenkel and Smit, 2001), as shown in equations (2) and (3).

$$\sigma_{ij} = \frac{\sigma_i + \sigma_j}{2} \quad (2)$$

$$\varepsilon_{ij} = \sqrt{\varepsilon_i \varepsilon_j} \quad (3)$$

Table 1. Lennard-Jones parameters of montmorillonite-water system applied in this work.

Species	Symbol	Charge (e)	ε (kcal/mol)	σ (Å)	Ref.
water hydrogen (SPC/E)	Hw	0.4238			a
water oxygen (SPC/E)	Ow	-0.8476	0.1554	3.1655	a
hydroxyl hydrogen	Ho	0.425			b
hydroxyl oxygen	Oh	-0.95	0.1554	3.1655	b
bridging oxygen	Ob	-1.05	0.1554	3.1655	b
bridging oxygen with octahedral substitution	Obos	-1.1808	0.1554	3.1655	b
bridging oxygen with tetrahedral substitution	Obts	-1.1688	0.1554	3.1655	b
hydroxyl oxygen with substitution	Ohs	-1.0808	0.1554	3.1655	b
tetrahedral silicon	Si	2.1	1.8405×10^{-6}	3.3020	b
octahedral aluminum	Al (ao)	1.575	1.3298×10^{-6}	4.2713	b
tetrahedral aluminum	Alt (at)	1.575	1.8405×10^{-6}	3.3020	b
octahedral magnesium	Mg	1.36	9.0298×10^{-7}	5.2643	b
aqueous sodium ion	Na	1	0.1301	2.35	c

a: (Berendsen et al., 1987); b: (Cygan et al., 2004); c: (Smith and Dang, 1994).

2.2. Relaxation and simulation details

MD simulations were carried out using LAMMPS (Plimpton, 1995) code. Three-dimensional periodic boundary condition was applied in the simulations. The van der Waals forces were calculated using the Lennard-Jones potential model with the cut-off radius set as 10 Å. Verlet algorithm (Frenkel et al., 1997) was applied to integrate the motion equations. Long-range electrostatic interactions with a cut-off radius of 8.5 Å were calculated using the Ewald sum method (Darden et al., 1993). The conjugate gradient method was used to do the energy minimization for geometry optimization, where the convergence tolerance was controlled at the energy of 1.0e-6

kcal/mol, the force of 1.0e-8 kcal/(mol•Å), and the maximum number of iteration steps of 1000.

To obtain a sufficient equilibrium configuration, the montmorillonite models were equilibrated with the micro-canonical (NVE) ensemble for 200 ps, followed by the canonical (NVT) ensemble for 200 ps, and then with the isothermal-isobaric (NPT) ensemble for 600 ps, respectively. The Nose-Hoover anisotropic thermostat and barostat were used to control temperature and pressure, with a temperature of 298 K and pressure of 1.0 atm. The time step of the whole simulation was set to 1.0 fs. Finally, the equilibrium systems were carried out to uniaxial tensile test along the *x*-, *y*- and *z*-directions (corresponding to [1 0 0], [0 1 0], and [0 0 1] crystal orientation), respectively. The uniaxial tensile test was achieved by changing the dimension of the simulation box of montmorillonite supercell, called as strain-controlled loading approach. While stretching along the *x*-direction, a certain strain rate was applied in this direction, with the temperature 298 K and the pressure 1 atm in the other two directions during the whole simulation. Stretching along the *y*- and *z*-directions was set in the same way.

To evaluate the effect of strain rate on the tensile mechanical properties of montmorillonite, the dehydrated montmorillonite was deformed at different strain rates (10×10^{-7} fs^{-1}, 5×10^{-7} fs^{-1}, 1×10^{-7} fs^{-1}, and 5×10^{-8} fs^{-1}). The evolution of stress with tensile strain along the *x*- and *z*-directions is illustrated in Figure S1 (it could be found in Supplementary Material). The decrease of critical strain and maximum stress with decreasing strain rate is found especially for stretching along the *x*-direction, but the difference between the cases of 5×10^{-8} fs^{-1} and 5×10^{-7} fs^{-1} was rather small. Moreover, there is almost no difference in all cases for tensile along the *z*-direction. Therefore, the tensile simulation ten times slower will not greatly change the simulation results, which agrees well with the results of the literature (Yang et al., 2019; Zhang et al., 2021). To ensure reliability and save the cost of computation time, the tensile strain rate of 5×10^{-7} fs^{-1} was selected to carry out the uniaxial tensile test for 600 ps to obtain a total strain of 0.3. In the tensile process, the relationship between stress and strain, as well as the trajectory file of deformation and failure processes, were

obtained.

3. Results and discussions

3.1. The atomic structure before loading

The basal spacing of different hydrated montmorillonite increases with water content, as shown in Table 2. The simulation results of montmorillonite in this work agree well with previous results. It illustrates the accuracy of the models and the applied force field.

Table 2**.** The basal spacing of different hydrated montmorillonite.

Water content (%)	Results in this work (Å)	Other simulation results (Å)	Experiments (Å)
0	9.616	9.51 ~ 10.01 [c,d]	9.55 e; 9.60~9.80 [f]
10	11.147	11.04 ~ 11.94 [d]	11.91 ~ 12.35 [f]
20	12.630	12.08 [g]; 12.3 [h]; 12.64 [i]; 12.32 [j]; 12.2 [k]; 12.0 [l]; 12.16 [a]; 12.55 [d]	12.0 ~ 12.6 [e,m,n,b]
30	14.090	13.09,14.75 [d]	-

a- (Zheng and Zaoui, 2011); b- (Keren R, 1975); c- (Kuang et al., 2013); d- (Chávez-Páez et al., 2001a); e- (Berend et al., 1995); f- (Fu et al., 1990); g- (Chang et al., 1995); h- (Marry et al., 2002); i- (Kosakowski et al., 2008); j- (Boek et al., 1995); k- (Chávez-Páez et al., 2001b); l- (Karaborni et al., 1996); m- (Porion et al., 2007); n- (Mooney et al., 1952).

The RDF and coordination number (CN) for atoms *j* around *i* were calculated respectively by:

$$g(r)_{ij} = \frac{n(r)_j}{\rho_j V} \approx \frac{n(r)_j}{4\pi\rho_j r^2 \Delta r} \quad (4)$$

$$\mathrm{CN}_{ij} = 4\pi\rho_j r^2 \int_0^{r_{ij}} g(r) r^2 dr \quad (5)$$

where $n(r)_j$ is the average number of atom *j* around *i* in a spherical shell of radius *r* to $r + \Delta r$. ρ_j is the number density of atom *j*. *r* is the distance between atoms *i* and *j*.

To understand the effect of water content on the atomic structure of montmorillonite sheet, the RDFs of Al-Ob, Ob-Hw (Figure 2), Al-Oh, and Si-Ob (Figure S2) of different hydrated montmorillonite were illustrated, where the $g(r)$ is the number of the atom pairs between given ranges of separation *r*. The intensity of first peak in these RDFs of Al-Ob, Al-Oh, and Si-Ob in

montmorillonite are positively correlated with water content, where the position of the first peak remains the same, which are 1.95 Å for Al-Ob and Al-Oh, 1.55 Å for Si-Ob. It indicates that the increasing water content could slightly rise the attraction between Al-Ob, Al-Oh, and Si-Ob atom pairs in clay layer structure. Figure 2(b) shows the radius of first peak in RDF of Ob-Hw declined with increasing water content, which may indicate that partial water molecules in the interlayer space are closer to the surface oxygen (Ob) of montmorillonite at a higher hydrated state.

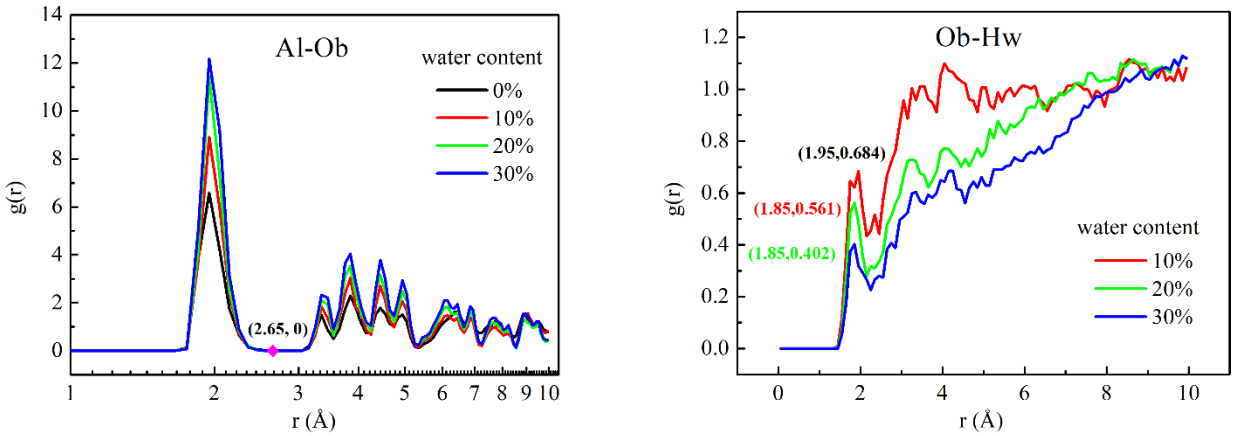

(a) (b)

Figure 2. Radial distribution function (RDF) of (a) Al-Ob; (b) Ob-Hw, in montmorillonite system.

To understand the coordination environments of montmorillonite-water system, the CNs of different atom pairs were calculated by integrating the RDF curves from origin to the first minimum based on equation (5). As shown in Table S1 and S2, the CNs of total Si-O and Al-O atom pairs for all hydrated cases are always equal to 4.0 and 6.0, respectively. This is consistent with the coordination number of Si-O and Al-O in silicon-oxygen tetrahedral and aluminum-oxygen octahedral sheets of clay. As shown in Table S3, at 0% ~ 20% hydrated cases, the CNs of Ob-Hw and Na-Ow rise with increasing water content, but that of Na-Ob decreases, which agrees well with the previous simulations for NH_4-montmorillonite (Peng et al., 2020) and Na-smectite (Zhang et al., 2014). With increasing water content, the Clay-Water (C…W) hydrogen bonds (HBonds) could be constantly generated by the hydrogen atoms (Hw) of interlayer water molecules and oxygen atoms

(Ob) of clay surface; and the interaction between interlayer cation Na^+ and clay surface could constantly reduce, and the partial Na^+ cations left clay surface and diffused into water. On the other hand, compared the 20% hydrated case with the 30% hydrated one, the CNs of Ob-Hw, Na-Ob, and Na-Ow were almost the same, indicating that the coordination of cation Na^+ by atoms Ow and Ob, as well as Ob and Hw were saturated and stable at 20% hydrated case (see Figure S3).

A bond-breakage criterion based on the RDFs of atom pairs was proposed by Yang et al. (Yang et al., 2019), that the first local minimum after the first peak of RDF curves means that the chance of finding atoms pairs with the corresponding separation distance is approximately zero. Thus, it could assume that the bonds would be broken once the increasing distance between atom pairs under strain is greater than this distance. As defined in CLAYFF force field, there are no bond between atoms except hydrogen and oxygen in hydroxyl and water molecules, in which exist the covalent bonds. As a difference, virtual bonds were defined here with the symbol "…" in Al…O, Al…Oh, Si…O, and O…H bonds in clay system, with their bond energy equal to the non-bonded interactions. The RDFs of Al-Ob, Al-Oh, and Si-Ob bonds for montmorillonite are shown in Figure 2 and Figure S2, and the cut-off distances of each virtual bond breakage are listed in Table 3. Additionally, the hydrated montmorillonite contains two types of HBonds: (1) the C…W HBonds (Clay-Water) is formed between water molecules and the acceptor oxygen of montmorillonite surface; (2) the W…W HBonds (Water-Water) is formed between water molecules. It is worth noting that the C…W HBonds play a more important role in the mechanical properties of montmorillonite than W…W HBonds, so the C…W HBonds would be considered in this study. The criterion for forming the HBonds is the cut-off distance O-H, as 2.4 Å, as proposed by Martí (Martí, 1999).

Table 3. The cut-off distance of individual bond types for Na-montmorillonite, compared with that of kaolinite in previous work (Yang et al., 2019).

Bond types	Cut-off distance (Å)

	Na-montmorillonite in this work	Kaolinite in previous work (Yang et al., 2019)
Al…Ob	2.65	2.74
Al…Oh	2.85	2.66
Si…Ob	1.85	1.84
C…W HBonds	2.4 (Martí, 1999)	3.0

230

231 **3.2. Influences of structural anisotropy and water content**

232 **3.2.1. Stress-strain relationship**

233 The maximum tensile stress of montmorillonite along the *x*-, *y*-, and *z*-directions decline as the
234 water content increases, as shown in Figure 3. The most critical decrease of the maximum tensile
235 stress was found from the dehydrated case to 10% hydrated cases of montmorillonite. The existence
236 of water greatly reduced the tensile mechanical strength of montmorillonite. Moreover, to further
237 analyze the deformation process of each stage in the stress-strain curve, point O referred to the initial
238 system without strain, point D for the final system with a strain of 0.3; and points A, B, and C were
239 the tensile strain states at the maximum stress, under failure, and residue respectively (Figure 3(a)).
240 Due to the fluctuations of stress while tensile along the *z*-direction, Savitzky-Golay method
241 (Gallagher, 2020) was performed to smooth the curves, as displayed in Figure 3(c).

242 As shown in Figure 3(a), during the stretching process along the *x*- and *y*-direction for all systems,
243 the stress increases almost linearly with strain from the initial state (point O) to maximum (point A).
244 Thereafter, a sharp drop occurs from maximum (point A) to relative lower value (point B), which
245 means a sudden and brittle failure. However, while stretching along the *z*-direction for hydrated
246 montmorillonite, the stress decreased relatively flat, which signified a good plastic (Figure 3(c)).
247 This indicates that the increase of water content for montmorillonite improves its plastic, which
248 agrees well with the experimental results of Zhang et al. (Zhang et al., 2012). Besides, the evolutions
249 of stress with strain were similar to the cases of dehydrated montmorillonite for stretching along the
250 *x*-, *y*, and *z*-directions, but the maximum stress along *z*-direction are much smaller than the others.

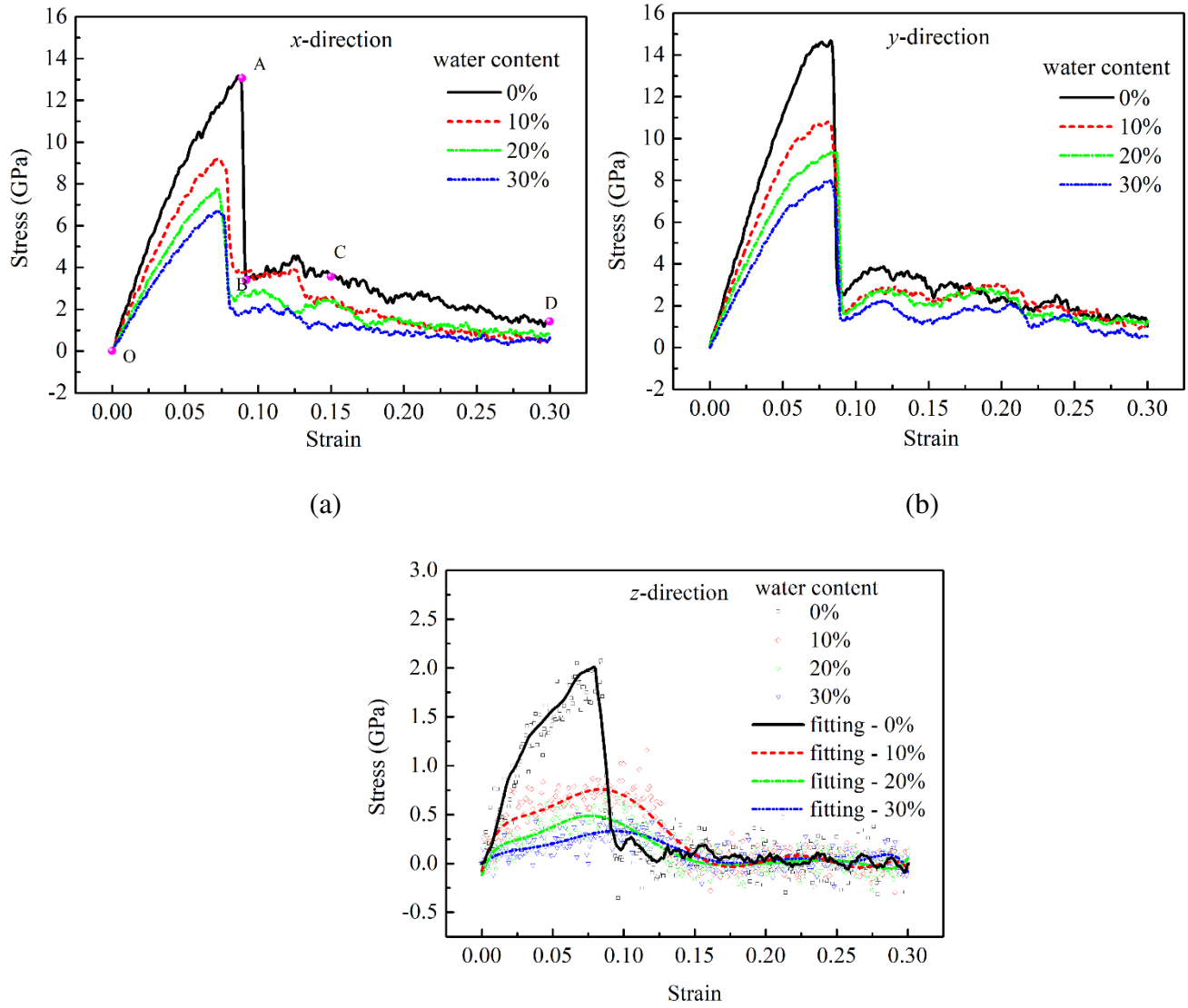

(a) (b)

(c)

Figure 3. Tensile stress-strain curves of Na-montmorillonite with different water contents at stretched along different directions: (a) *x*-direction; (b) *y*-direction; (c) *z*-direction, where fitting curves are obtained by Savitzky-Golay method to perform smooth.

3.2.2. Broken bonds during the failure process

The normalization number of broken bonds (r_{bond}) of hydrated montmorillonite could be calculated by the following equation.

$$r_{\mathrm{bond}} = \frac{N-N_0}{N_0} \times 100\% = \frac{\Delta N}{N_0} \times 100\% \quad (6)$$

where N and N_0 are the numbers of the certain bond at the state corresponding to a certain strain and the initial strain 0, respectively.

Since the deformation behavior of different hydrated montmorillonite were very similar, the montmorillonite with a water content of 10% was taken thereafter for analysis. The deformation of hydrated montmorillonite with water content of 10% under tensile along the *x*-direction (Figure 4(a)) could be divided into four stages: (1) at OA stage, no bond in the crystal structure was broken when the tensile strain was less than 0.05. Thereafter, just very few bonds were broken as the tensile strain increased to ultimate tensile strain (Point A). (2) At AB stage, the largest number of bonds were broken, and the crack grew rapidly. The clay sheets were seriously destroyed. (3) At BC stage, the number of broken bonds for Al…Ob and Al…Oh rose slowly with tensile strain, accompanied by further propagation of the crack and hole. However, the Si…Ob bonds were not further damaged. (4) At CD stage, the number of broken bonds for Al…Ob and Al…Oh fluctuated around a certain value, and the one of Si…Ob remained unchanged.

As shown in Figure 4(a) and (b), the number of broken bonds for Al…Ob is greater than that of Al…Oh as stretching along the *x*-direction, but it is just the opposite as stretching along the *y*-direction. In both cases, the broken bonds of Si…Ob remained the weakest, compared with the other two bond types. The normalized number of broken bonds of Al…Ob and Si…Ob was approximately the same when stretching along the *x*- and *y*-direction. However, the normalized number of broken bonds of Al…Oh in the *y*-direction was much greater than that of *x*-direction, which was due to the different arrange for Al…Oh bond along the *x*- and *y*-directions (Figure S4), shown as the more total broken bonds in the *y*-direction. Therefore, more energy was required to overcome the interaction of these bonds as stretching along the *y*-direction, so the tensile mechanical strength of *y*-direction for montmorillonite was superior to that of *x*-direction. This finding also could explain why the tensile mechanical strength of *y*-direction is greater than the one of *x*-direction for kaolinite (Han et al., 2019; Yang et al., 2019; Zhang et al., 2021).

As shown in Figure 4(c), the layers of montmorillonite system are delaminated at the tensile process along the *z*-direction, and the tetrahedra and octahedra sheets remain unchanged, which agrees well with the results of the literature (Zhang et al., 2021). The maximum stress in the stress-strain curve of *z*-direction was much smaller than that of *x*-direction and *y*-direction (Figure 3), due to the weaker interactions between layers. Moreover, (1) at OA stage, with increasing tensile strain, the number of broken bonds for C…W HBonds rose significantly. It was due to the primary interaction between layers by C…W HBonds. With the increasing tensile strain, the distance between the surface of montmorillonite and interlayer water increased, causing the broken bonds for C…W Hbonds. (2) At AB and BC stage, the number of broken bonds for C…W HBonds declined rapidly. The layers of montmorillonite system was delaminated as two portions, the water molecules around the division layer of clay sheet moved gradually close to the surface of montmorillonite, resulting in the forming bonds for C…W HBonds. (3) At CD stage, the number of broken bonds for C…W HBonds fluctuated around a certain value, indicating that the montmorillonite system was separated into two portions, and then into an equalized state.

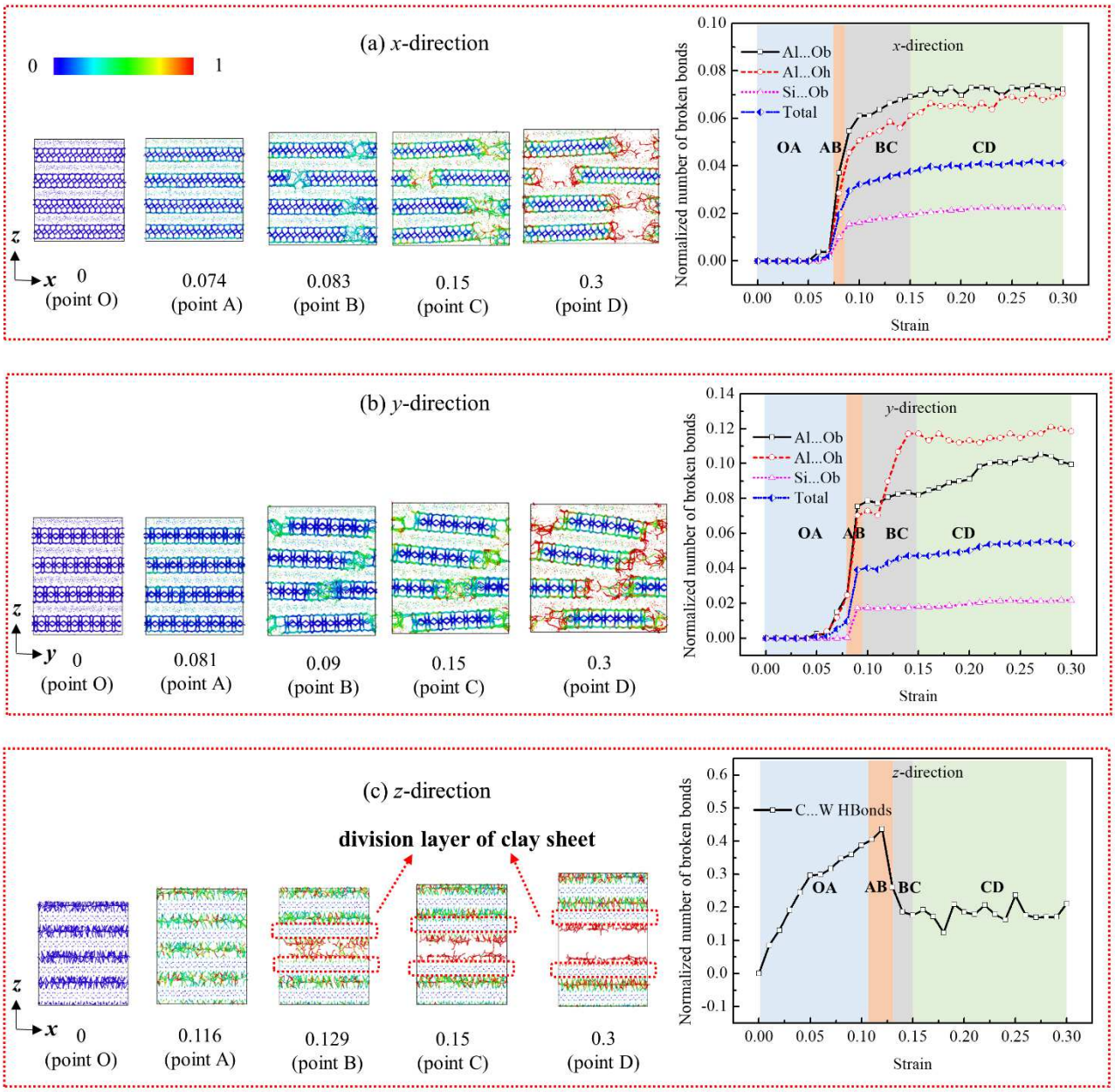

Figure 4. Evolution of structure deformation and the normalization number of broken bonds of hydrated montmorillonite with water content of 10% under different tensile strains: (a), (b) The Al…Ob, Al…Oh, and Si…Ob bonds are considered, stretching along *x*-direction and *y*-direction, respectively; (c) The C…W HBonds are analyzed, stretching along *z*-direction. The color code marks the bonds with less deformation as blue and those with more deformation as red.

To study the effect of water content and structural anisotropy on the evolution of broken bonds, the relationship between the total normalization number of broken bonds and tensile strains for different

hydrated montmorillonite are shown in Figure 5. As for dehydrated montmorillonite (water content 0%), no C…W HBond was contained, so the 0% curve was not shown in Figure 5(c). As shown in Figure 5(b), as stretching along the *y*-direction, the normalized number of total broken bonds under different hydrated states are relatively closed. However, in Figure 5(a) and (c), the lower the water content, the more the broken bonds. On the other hand, the normalized number of total broken bonds in the *y*-direction was superior to the *x*-direction in all cases. This evolution of broken bonds further shows the structural anisotropy of montmorillonite, especially in the parallel (*x*- and *y*-) and perpendicular (*z*-) directions.

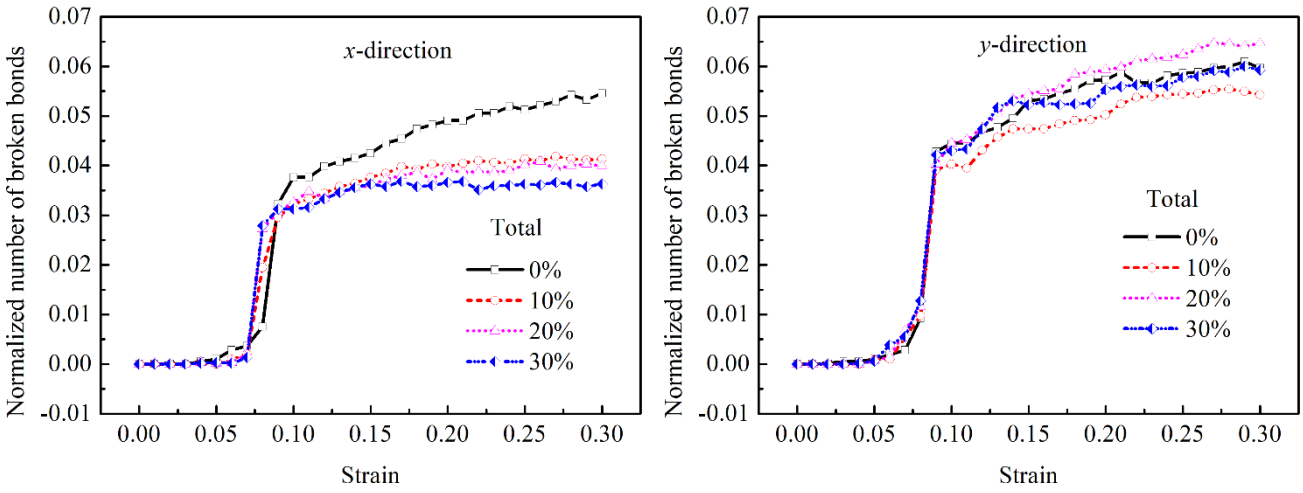

(a) (b)

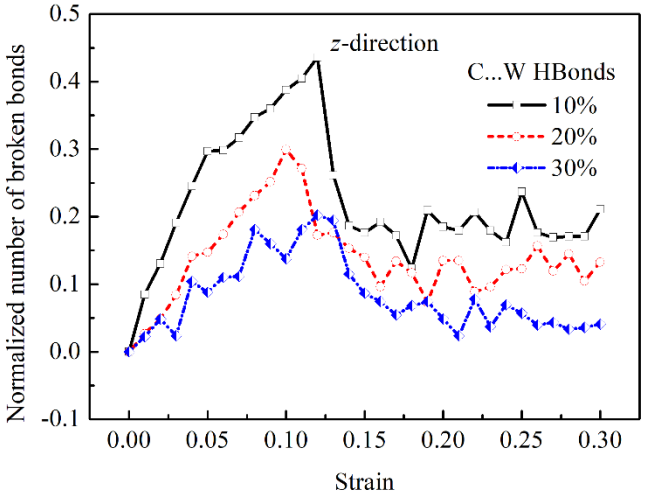

(c)

Figure 5. Evolution of (total) normalization number of broken bonds of different hydrated

montmorillonite with tensile strains: (a) total bonds for *x*-direction, and (b) *y*-direction; (c) C…W HBonds for *z*-direction.

3.2.3. Tensile mechanical parameters

The ultimate tensile strength and ultimate tensile strain are equal to the maximum stress and its corresponding strain on the stress-strain curve, and the residual tensile strength is the stress at a strain of 0.3 (Figure 3). Young's modulus could be obtained by taking the slope of the linear elastic regime with a small strain range, where the selected strain range is 0 ~ 0.01. Based on the ultimate tensile strength of three directions, the overall ultimate tensile strength (σ_{toverall}) is proposed to illustrate the overall tensile mechanical, computed by equation (7).

$$\sigma_{\text{toverall}} = \sqrt{\frac{\sigma^2_{tx} + \sigma^2_{ty} + \sigma^2_{tz}}{3}} \tag{7}$$

Where σ_{tx}, σ_{ty}, and σ_{tz} correspond to the ultimate tensile strength of the *x*-, *y*-, and *z*-directions, respectively. Similarly, the overall Young's modulus (E_{overall}) could be determined.

Young's modulus of dehydrated montmorillonite and previous results, have been collected in Table 4, reflecting the binding strength among atoms or molecules in nanoscale. The simulation results in this study agreed well with the results of the previous literature (Ledbetter et al., 2001; Chen and Evans, 2006; Nazmul et al., 2008; Zheng and Zaoui, 2018), which could validate the accuracy of applied force field and established model. There is a certain difference in the value of Young's modulus between this work and previous studies, likely due to the difference in ion substitution site, the applied force field, and selecting ensemble for montmorillonite during whole simulations. Furthermore, the sequence of Young's modulus for dehydrated montmorillonite was $y > x > z$, which is consistent with results found by Zheng and Zaoui (Zheng and Zaoui, 2018), for the cases before swelling and after shrinking of montmorillonite.

Table 4. Young's modulus (GPa) of dehydrated Na-montmorillonite compared to previous experimental and simulation results.

Direction	Results in this work	Other simulation results	DFT	Experiments	Theoretical derivation value
x	208.92	246 (Before swelling) [e]; 197 (After shrinking) [e]; 235 (0 K) [g]; 221 (300 K) [g];	178.4 ± 2.7 (pyrophyllite) [f];	222 [h]; 6.2 [i]; ~ 60 [c]; 32.9 [a]; 49 (pyrophyllite) [c]	178 ~265 [c]; 255 [b]; 54.56 [d]
y	237.66	251 (Before swelling) [e]; 249 (After shrinking) [e]; 218 (0K) [g]; 210 (300K) [g];	166.8 ± 2.5 (pyrophyllite) [f];		
z	29.85	15 (Before swelling) [e]; 11.5 (After shrinking) [e];	69.2 ± 4.8 (pyrophyllite) [f];		

a- (Nazmul et al., 2008); b- (Manevitch and Rutledge, 2004); c- (Chen and Evans, 2006); d- (Katti et al., 2005); e- (Zheng and Zaoui, 2018); f- (Zartman et al., 2010); g- (Carrier et al., 2014); h- (Ledbetter et al., 2001); i- (Prasad, 2001).

The intensity attenuation coefficient (D_s) of the sample is used to illustrate its post-peak strength decay behavior, proposed by Peng et al. (Peng et al., 2015), which can be expressed as:

$$D_s = \frac{\sigma_t - \sigma_r}{\sigma_t} \tag{8}$$

where σ_t represents the ultimate tensile strength (corresponding to point A in stress-strain curve of Figure 3(a)), and σ_r represents the residual tensile strength (point D in Figure 3(a)).

As shown in Figure 6 and Table 5, the ultimate tensile strength and Young's modulus of montmorillonite decrease almost linearly with increasing water content. It indicates that the existence of water reduced the capability to resist deformation and failure of montmorillonite. For all cases, the ultimate tensile strength, Young's modulus, and residual tensile strength along the *y*-direction are slightly superior to those along the *x*-direction, and significantly superior to those along the *z*-direction. At 0% ~ 20% hydrated cases, the intensity attenuation coefficient along *z*-direction were close to 1.0, and greater than that of *x*- and *y*-direction (Table 5), illustrating that the tensile

mechanical strength of *z*-direction decayed the most. Moreover, there was still residual tensile strength for *y*- and *x*- directions at the strain of 0.3. These findings indicated that the weakest surface of montmorillonite is (0 0 1) crystal plane, which is consistent with some previous work on montmorillonite (Zheng and Zaoui, 2018) and kaolinite (Zhang et al., 2021). It further provides evidence for the anisotropy of mechanical properties of montmorillonite.

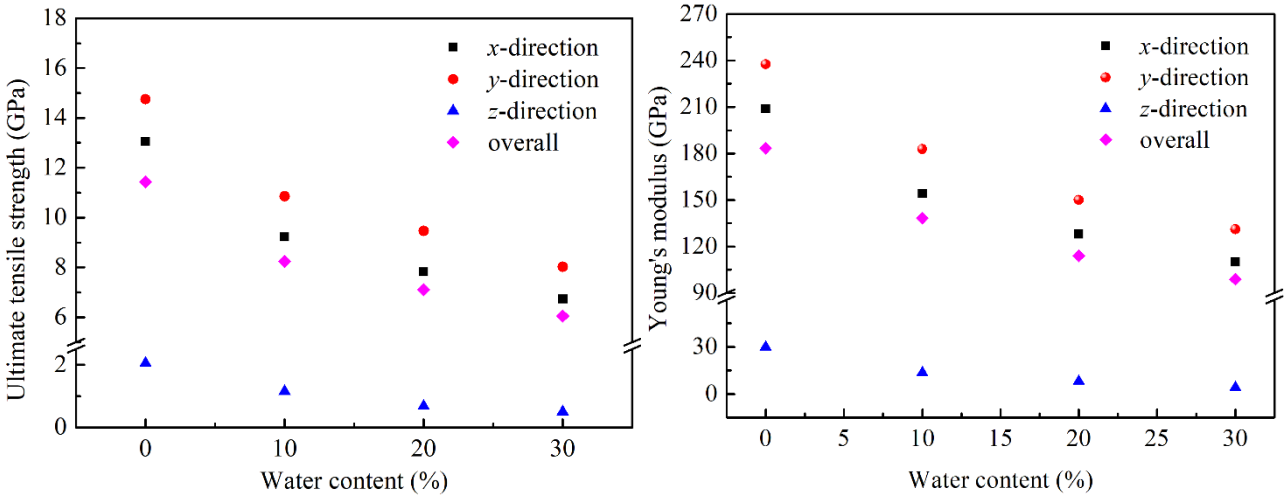

(a) (b)

Figure 6. Evolution of tensile mechanical parameters with water content for montmorillonite, corresponding to *x*-, *y*-, *z*-, and overall directions: (a) ultimate tensile strength; (b) Young's modulus.

Table 5. Residual tensile strength and intensity attenuation coefficient of different hydrated montmorillonite.

Water content (%)	Residual tensile strength (GPa)			Intensity attenuation coefficient		
	x	*y*	*z*	*x*	*y*	*z*
0	1.36	1.38	0.01	0.90	0.91	1.00
10	0.53	1.05	0.00	0.94	0.90	1.00
20	0.76	1.19	0.00	0.90	0.87	0.99
30	0.52	0.54	0.05	0.92	0.93	0.91

4. Conclusions

Molecular dynamics (MD) simulations have been used to study the effect of water content and structural anisotropy on atomic structure and tensile mechanical properties of montmorillonite in

three directions. It is noted that the CLAYFF force field cannot present the bond breaking and rearrangement, so the bond-breakage criterion based on radial distribution function (RDF) of atom pairs was proposed to describe the deformation and failure process of montmorillonite.

The Young's modulus of dehydrated montmorillonite and basal spacing of all hydrated montmorillonite obtained in this work were consistent with previous simulation and experiment results. The increasing water content augmented the first peak in RDFs of Al-Ob, Al-Oh, and Si-Ob, but without effect on the position of these peaks, illustrating that the higher water content could slightly rise the attraction between Al-Ob, Al-Oh, and Si-Ob atom pairs in clay layer structure. Moreover, stretching along the *x*- and *y*-directions, the Al…Ob and Al…Oh bonds were broken earlier and significant higher quantities than the Si…Ob bonds, indicating that the silicon-oxygen tetrahedral sheets was stronger than aluminum-oxygen octahedral sheet. The normalized number of total broken bonds in the *y*-direction was superior to the *x*-direction. On the other hand, stretching along *z*-direction, the layers of the system were delaminated, where Clay-Water hydrogen bonds (HBonds) was broken for the hydrated system, while the tetrahedral and octahedral sheets remained intact. Furthermore, the higher the water content, the greater the plasticity of the montmorillonite system. Additionally, based on Young's modulus, ultimate tensile strength, and residual tensile strength of three directions, the sequence of tensile mechanical strength for montmorillonite was $y > x > z$, showing obvious anisotropy of montmorillonite. The increase of water molecules for montmorillonite gradually reduced its tensile mechanical properties. This work could lay the foundation for further research on the compression and shear mechanical properties of clay minerals. Especially, the mechanical properties of clay are also sensitive to water under compression, which will be further discussed in the future.

Acknowledgments

This research was financially supported by the National Natural Science Foundation of China

(Grant No. 52009149), the Natural Science Foundation of GuangDong Basic and Applied Basic Research Foundation (Grant No. 2021A1515012612), and the China Scholarship Council (202106380147) for Mr. Pengchang WEI.

Notes

The authors declare no competing financial interest.

Author statement

Peng-Chang Wei: Conceptualization, Methodology, Investigation, Data Curation, Writing - Review & Editing, Writing - Original Draft, Visualization;

Yuan-Yuan Zheng: Conceptualization, Writing-Review & Editing, Supervision; Project administration；

Yong Xiong: Methodology; Software;

Sheng-Biao Zhou: Software;

Kamal Al-zaoari: Visualization;

Ali Zaoui: Writing - Review & Editing.

References:

Al-Zaoari, K., Zheng, Y., Wei, P., Zhang, L. and Yin, Z., 2022. Early stage of swelling process of dehydrated montmorillonite through molecular dynamics simulation. Mater. Chem. Phys., 283, 126015. http://doi.org/10.1016/j.matchemphys.2022.126015.

Benazzouz, B. K. and Zaoui, A., 2012. A nanoscale simulation study of the elastic behaviour in kaolinite clay under pressure. Mater. Chem. Phys., 132, 880-888. http://doi.org/10.1016/j.matchemphys.2011.12.028.

Berend, I. et al., 1995. Mechanism of adsorption and desprotion of water vapor by homoionic montmorillonites. II: The Li+, Na+, K+, Rb+, and Cs+-exchanged forms. Clay Clay Miner., 43, 324-336. http://doi.org/10.1346/CCMN.1995.0430307.

Berendsen, H. J. C., Grigera, J. R. and Straatsma, T. P., 1987. The missing term in effective pair potentials. J. Phys. Chem., 91, 6269-6271. http://doi.org/10.1021/j100308a038.

Bobko, C. and Ulm, F., 2008. The nano-mechanical morphology of shale. Mech. Mater., 40, 318-337. http://doi.org/10.1016/j.mechmat.2007.09.006.

Boek, E. S., Coveney, P. V. and Skipper, N. T., 1995. Monte Carlo Molecular Modeling Studies of Hydrated Li-, Na-, and K-Smectites: Understanding the Role of Potassium as a Clay Swelling Inhibitor. J. Am. Chem. Soc., 117, 12608-12617. http://doi.org/10.1021/ja00155a025.

Carrier, B., Vandamme, M., Pellenq, R. J. M. and Van Damme, H., 2014. Elastic Properties of Swelling Clay Particles at Finite Temperature upon Hydration. J. Phys. Chem. C, 118, 8933-8943. http://doi.org/10.1021/jp412160e.

Chang, F. C., Skipper, N. T. and Sposito, G., 1995. Computer Simulation of Interlayer Molecular Structure in Sodium Montmorillonite Hydrates. Langmuir, 11, 2734-2741. http://doi.org/10.1021/la00007a064.

Chávez-Páez, M., Van Workum, K., de Pablo, L. and de Pablo, J. J., 2001a. Monte Carlo simulations of Wyoming sodium montmorillonite hydrates. The Journal of Chemical Physics, 114, 1405-1413. http://doi.org/10.1063/1.1322639.

Chávez-Páez, M., Van Workum, K., de Pablo, L. and de Pablo, J. J., 2001b. Monte Carlo simulations of Wyoming sodium montmorillonite hydrates. The Journal of chemical physics, 114, 1405-1413. http://doi.org/10.1063/1.1322639.

Chen, B. and Evans, J. R. G., 2006. Elastic moduli of clay platelets. Scripta Mater., 54, 1581-1585. http://doi.org/10.1016/j.scriptamat.2006.01.018.

Cygan, R. T., Liang, J. and Kalinichev, A. G., 2004. Molecular Models of Hydroxide, Oxyhydroxide, and Clay Phases and the Development of a General Force Field. J. Phys. Chem. B, 108, 1255-1266. http://doi.org/10.1021/jp0363287.

Darden, T., York, D. and Pedersen, L., 1993. Particle mesh Ewald: An N·log(N) method for Ewald

457 sums in large systems. J. Chem. Phys., 98, 10089-10092. http://doi.org/10.1063/1.464397.
458 Ebrahimi, D., Pellenq, R. J. M. and Whittle, A. J., 2012. Nanoscale Elastic Properties of
459 Montmorillonite upon Water Adsorption. Langmuir, 28, 16855-16863.
460 http://doi.org/10.1021/la302997g.
461 Frenkel, D. and Smit, B., 2001. Understanding molecular simulation: From algorithms to
462 applications. Academic Press. http://doi.org/10.1016/B978-012267351-1/50012-2.
463 Frenkel, D., Smit, B., Tobochnik, J., McKay, S. R. and Christian, W., 1997. Understanding
464 Molecular Simulation. Comput. Phys., 11, 351. http://doi.org/10.1063/1.4822570.
465 Fu, M. H., Zhang, Z. Z. and Low, P. F., 1990. Changes in the Properties of a Montmorillonite-Water
466 System during the Adsorption and Desorption of Water: Hysteresis1. Clays & Clay Minerals, 38,
467 485-492. http://doi.org/10.1346/CCMN.1990.0380504.
468 Gallagher, N., 2020. Savitzky-Golay Smoothing and Differentiation Filter, Eigenvector Research
469 Inc.: Manson, WA.
470 https://www.researchgate.net/publication/338518012_Savitzky-Golay_Smoothing_and_Differentiat
471 ion_Filter
472 Han, Z., Yang, H. and He, M., 2019. A molecular dynamics study on the structural and mechanical
473 properties of hydrated kaolinite system under tension. Materials Research Express, 6, 850
474 . http://doi.org/10.1088/2053-1591/ab2562.
475 Hantal, G. et al., 2014. Atomic-scale modelling of elastic and failure properties of clays. Mol. Phys.,
476 112, 1294-1305. http://doi.org/10.1080/00268976.2014.897393.
477 Hedan, S. et al., 2015. Measurement of the elastic properties of swelling clay minerals using the
478 digital image correlation method on a single macroscopic crystal. Appl. Clay Sci., 116-117,
479 248-256. http://doi.org/10.1016/j.clay.2015.04.002.
480 Hueckel, T., 2002. Reactive plasticity for clays during dehydration and rehydration. Part 1: concepts
481 and options. Int. J. Plasticity, 18, 281-312. http://doi.org/10.1016/S0749-6419(00)00099-1.

Húlan, T. et al., 2015. Development of Young's Modulus of Illitic Clay during Heating up to 1100 °C. Mater. Sci.+, 21, 429-434. http://doi.org/10.5755/j01.ms.21.3.7152.

Karaborni, S., Smit, B., Heidug, W., Urai, J. and Oort, E. V., 1996. The Swelling of Clays: Molecular Simulations of the Hydration of Montmorillonite. Science, 271, 1102-1104. http://doi.org/10.1126/science.271.5252.1102.

Katti, D. R., Schmidt, S. R., Ghosh, P. and Katti, K. S., 2005. Modeling the response of pyrophyllite interlayer to applied stress using steered molecular dynamics. Clays Clay Miner., 53, 171-178. http://doi.org/10.1346/CCMN.2005.0530207.

Katti, D. R., Schmidt, S. R., Ghosh, P. and Katti, K. S., 2007. Molecular modeling of the mechanical behavior and interactions in dry and slightly hydrated sodium montmorillonite interlayer. Can. Geotech. J., 44, 425-435. http://doi.org/10.1139/T06-127.

Keren R, S. I., 1975. Water vapor isotherms and heat of immersion of Na/Ca-montmorillonite systems; I, Homoionic clay. Clays & Clay Minerals, 23, 193-200. http://doi.org/10.1346/CCMN.1975.0230305.

Kosakowski, G., Churakov, S. V. and Thoenen, T., 2008. Diffusion of Na and Cs in montmorillonite. Clays Clay Miner., 56, 190-206. http://doi.org/10.1346/CCMN.2008.0560205.

Kuang, L., Zhou, G., Shang, X. and Zhao, X., 2013. molecular dynamic simulation of interlayer water structure in Na-montmorillonite. journal of china coal society, 38, 418-423. http://doi.org/CNKI:SUN:MTXB.0.2013-03-016.

Ledbetter, H. et al., 2001. Elastic constants of mullite containing alumina platelets. J. Eur. Ceram. Soc., 21, 2569-2576. http://doi.org/https://doi.org/10.1016/S0955-2219(01)00269-2.

Liu, Z. B., Xie, S. Y., Shao, J. F. and Conil, N., 2015. Effects of deviatoric stress and structural anisotropy on compressive creep behavior of a clayey rock. Appl. Clay Sci., 114, 491-496. http://doi.org/10.1016/j.clay.2015.06.039.

Liu, Z., Shao, J., Xie, S., Conil, N. and Talandier, J., 2019. Mechanical Behavior of Claystone in

507 Lateral Decompression Test and Thermal Effect. Rock Mech. Rock Eng., 52, 321-334.
508 http://doi.org/10.1007/s00603-018-1573-3.
509 Manevitch, O. L. and Rutledge, G. C., 2004. Elastic Properties of a Single Lamella of
510 Montmorillonite by Molecular Dynamics Simulation. J. Phys. Chem. B, 108, 1428-1435.
511 http://doi.org/10.1021/jp0302818.
512 Marry, V., Turq, P., Cartailler, T. and Levesque, D., 2002. Microscopic simulation of structure and
513 dynamics of water and counterions in a monohydrated montmorillonite. The Journal of Chemical
514 Physics, 117, 3454-3463. http://doi.org/10.1063/1.1493186.
515 Martí, J., 1999. Analysis of the hydrogen bonding and vibrational spectra of supercritical model
516 water by molecular dynamics simulations. J. Chem. Phys., 110, 6876-6886.
517 http://doi.org/10.1063/1.478593.
518 Mazo, M. A. et al., 2008. Molecular Dynamics Simulation of Thermomechanical Properties of
519 Montmorillonite Crystal. 3. Montmorillonite Crystals with PEO Oligomer Intercalates. J. Phys.
520 Chem. B, 112, 3597-3604. http://doi.org/10.1021/jp076028f.
521 Mcneil, L. E. and Grimsditch, M., 1993. Elastic moduli of muscovite mica. Journal of Physics
522 Condensed Matter, 5, 1681-1690. http://doi.org/10.1088/0953-8984/5/11/008.
523 Militzer, B., Wenk, H. R., Stackhouse, S. and Stixrude, L., 2010. First-principles calculation of the
524 elastic moduli of sheet silicates and their application to shale anisotropy. Am. Mineral., 96,
525 125-137. http://doi.org/10.2138/am.2011.3558.
526 Mooney, R. W., Keenan, A. G. and Wood, L. A., 1952. Adsorption of Water Vapor by
527 Montmorillonite. I. Heat of Desorption and Application of BET Theory1. J. Am. Chem. Soc., 74,
528 1367-1371. http://doi.org/10.1021/ja01126a001.
529 Nazmul, H. M., Jens, J. and Bjorlykke, K., 2008. Elastic properties of clay minerals. Leading Edge,
530 26, 758−770. http://doi.org/10.1190/1.2944161.
531 Ortega, J. A., Ulm, F. and Abousleiman, Y., 2007. The effect of the nanogranular nature of shale on

their poroelastic behavior. Acta Geotech., 2, 155-182. http://doi.org/10.1007/s11440-007-0038-8.

Peng, C. et al., 2020. Molecular dynamics simulation of NH4-montmorillonite interlayer hydration: Structure, energetics, and dynamics. Appl. Clay Sci., 195, 105657. http://doi.org/10.1016/j.clay.2020.105657.

Peng, J., Rong, G., Cai, M. and Peng, K., 2015. Determination of residual strength of rocks by a brittle index. Rock and Soil Mechanics, 36, 403-408. http://doi.org/10.16285/j.rsm.2015.02.015.

Plimpton, S., 1995. Fast Paraller Algorithms for Short-Range Molecular Dynamics. J. Comput. Phys., 117, 1-19. http://doi.org/10.1006/jcph.1995.1039.

Porion, P., Michot, L. J., Faugere, A. M. and Delville, A., 2007. Structural and dynamical properties of the water molecules confined in dense clay sediments: A study combining H-2 NMR spectroscopy and multiscale numerical modeling. J. Phys. Chem. C, 111, 5441-5453. http://doi.org/10.1021/jp067907p.

Prasad, M., 2001. Mapping impedance microstructures in rocks with acoustic microscopy. The Leading Edge, 20, 172-179. http://doi.org/10.1190/1.1438902.

Sato, H., 2005. First-principles studies on the elastic constants of a 1:1 layered kaolinite mineral. Am. Mineral., 90, 1824-1826. http://doi.org/10.2138/am.2005.1832.

Schmidt, S. R., Katti, D. R., Ghosh, P. and Katti, K. S., 2005. Evolution of Mechanical Response of Sodium Montmorillonite Interlayer with Increasing Hydration by Molecular Dynamics. Langmuir, 21, 8069-8076. http://doi.org/10.1021/la050615f.

Seppälä, A., Puhakka, E. and Olin, M., 2016. Effect of layer charge on the crystalline swelling of Na+ , K+and Ca2+ montmorillonites: DFT and molecular dynamics studies. Clay Miner., 51, 197-211. http://doi.org/10.1180/claymin.2016.051.2.07.

Smith, D. E. and Dang, L. X., 1994. Computer simulations of NaCl association in polarizable water. The Journal of chemical physics, 100, 3757-3766. http://doi.org/10.1063/1.466363.

Stixrude, L. and Peacor, D. R., 2002. First-principles study of illite-smectite and implications for clay

557 mineral systems. Nature, 420, 165-8. http://doi.org/10.1038/nature01155.
558 Suter, J. L., Coveney, P. V., Greenwell, H. C. and Thyveetil, M., 2007. Large-Scale Molecular
559 Dynamics Study of Montmorillonite Clay: Emergence of Undulatory Fluctuations and
560 Determination of Material Properties. J. Phys. Chem. C, 111, 8248-8259.
561 http://doi.org/10.1021/jp070294b.
562 Teich-McGoldrick, S. L., Greathouse, J. A. and Cygan, R. T., 2012. Molecular Dynamics
563 Simulations of Structural and Mechanical Properties of Muscovite: Pressure and Temperature
564 Effects. J. Phys. Chem. C, 116, 15099-15107. http://doi.org/10.1021/jp303143s.
565 Vanorio, T., Prasad, M. and Nur, A., 2003. Elastic properties of dry clay mineral aggregates,
566 suspensions and sandstones. Geophys. J. Int, 155, 319-326.
567 http://doi.org/10.1046/j.1365-246X.2003.02046.x.
568 Viani, A., Gualtieri, A. F. and Artioli, G., 2002. The nature of disorder in montmorillonite by
569 simulation of X-ray powder patterns. Am. Mineral., 87, 966-975.
570 http://doi.org/10.2138/am-2002-0720.
571 Wei, P. et al., 2021. Nanoscale friction characteristics of hydrated montmorillonites using molecular
572 dynamics. Appl. Clay Sci., 210, 106155. http://doi.org/10.1016/j.clay.2021.106155.
573 Wei, P., Zhuang, D., Zheng, Y., Zaoui, A. and Ma, W., 2022. Temperature and pressure effect on
574 tensile behavior of ice-Ih under low strain rate: A molecular dynamics study. J. Mol. Liq., 355,
575 118945. http://doi.org/10.1016/j.molliq.2022.118945.
576 Wenk, H., Lonardelli, I., Franz, H., Nihei, K. and Nakagawa, S., 2007. Preferred orientation and
577 elastic anisotropy of illite-rich shale. Geophysics, 72, 69-75. http://doi.org/10.1190/1.2432263.
578 Wu, Y. et al., 2020. Multiscale elastic anisotropy of a shale characterized by cross-scale big data
579 nanoindentation. Int. J. Rock Mech. Min., 134, 104458.
580 http://doi.org/10.1016/j.ijrmms.2020.104458.
581 Yang, H., He, M., Lu, C. and Gong, W., 2019. Deformation and failure processes of kaolinite under

582 tension: Insights from molecular dynamics simulations. Sci. China Phys. Mech. Astron., 62,
583 064612. http://doi.org/10.1007/s11433-018-9316-3.
584 Yotsuji, K., Tachi, Y., Sakuma, H. and Kawamura, K., 2021. Effect of interlayer cations on
585 montmorillonite swelling: Comparison between molecular dynamic simulations and experiments.
586 Appl. Clay Sci., 204, 106034. http://doi.org/10.1016/j.clay.2021.106034.
587 Zartman, G. D., Liu, H., Akdim, B., Pachter, R. and Heinz, H., 2010. Nanoscale Tensile, Shear, and
588 Failure Properties of Layered Silicates as a Function of Cation Density and Stress. J. Phys. Chem.
589 C, 114, 1763-1772. http://doi.org/10.1021/jp907012w.
590 Zhang, F., Xie, S. Y., Hu, D. W., Shao, J. F. and Gatmiri, B., 2012. Effect of water content and
591 structural anisotropy on mechanical property of claystone. Appl. Clay Sci., 69, 79-86.
592 http://doi.org/10.1016/j.clay.2012.09.024.
593 Zhang, L., Lu, X., Liu, X., Zhou, J. and Zhou, H., 2014. Hydration and Mobility of Interlayer Ions of
594 (Nax, Cay)-Montmorillonite: A Molecular Dynamics Study. J. Phys. Chem. C, 118, 29811-29821.
595 http://doi.org/10.1021/jp508427c.
596 Zhang, L., Zheng, Y., Wei, P., Diao, Q. and Yin, Z., 2021. Nanoscale mechanical behavior of
597 kaolinite under uniaxial strain conditions. Appl. Clay Sci., 201, 105961.
598 http://doi.org/10.1016/j.clay.2020.105961.
599 Zheng, Y. and Zaoui, A., 2011. How water and counterions diffuse into the hydrated montmorillonite.
600 Solid State Ionics, 203, 80-85. http://doi.org/10.1016/j.ssi.2011.09.020.
601 Zheng, Y. and Zaoui, A., 2018. Mechanical behavior in hydrated Na-montmorillonite clay. Phys. A.,
602 505, 582-590. http://doi.org/10.1016/j.physa.2018.03.093.
603 Zheng, Y., Zaoui, A. and Shahrour, I., 2011. A theoretical study of swelling and shrinking of
604 hydrated Wyoming montmorillonite. Appl. Clay Sci., 51, 177-181.
605 http://doi.org/10.1016/j.clay.2010.10.027.
606 Zhu, L., Shen, W., Shao, J. and He, M., 2021. Insight of molecular simulation to better assess

607 deformation and failure of clay-rich rocks in compression and extension. Int. J. Rock Mech. Min.,
608 138, 104589. http://doi.org/10.1016/j.ijrmms.2020.104589.

Graphical Abstract